crystals

MDPI

Article

Tailoring the Synthesis of Highly Tetragonal $BaTiO_3$ Nanoparticles by Regulating Aging Time and Calcination Temperature Using Sol–Gel Route

Sheng Liu [1], Yi-Hua Sun [1,2,3,*], Dong Zhang [1], Ye Yuan [1], Liao Lu [1], Xiao-Peng Jia [1], Hong-Wei Lin [1] and Hao-Xiang Zhang [1]

[1] Key Laboratory of Inorganic Nonmetallic Crystalline and Energy Conversion Materials, College of Materials and Chemical Engineering, China Three Gorges University, Yichang 443002, China; 202308560021011@ctgu.edu.cn (S.L.); zhangdong@ctgu.edu.cn (D.Z.); 202308560021018@ctgu.edu.cn (Y.Y.); 202408560021601@ctgu.edu.cn (L.L.); 202408560021596@ctgu.edu.cn (X.-P.J.); 202408050021579@ctgu.edu.cn (H.-W.L.); 202508020021047@ctgu.edu.cn (H.-X.Z.)
[2] Hubei Three Gorges Laboratory, Yichang 443007, China
[3] College of Mechanical and Power Engineering, Hubei Engineering Research Center for Graphite Additive Manufacturing Technology and Equipment, China Three Gorges University, Yichang 443002, China
* Correspondence: sunny.hust@ctgu.edu.cn; Tel.: +86-13872496451

Abstract

High-quality $BaTiO_3$ nanopowders were synthesized via a sol–gel method using butyl titanate and barium serving as precursors. This study systematically investigates the influence of calcination temperature (600–1000 °C) and gel aging time (2–10 h) on the phase evolution and microstructure of the nanoparticles. A pure tetragonal phase with a high tetragonality (c/a ratio of 1.0100) and an average particle size of 140 nm was achieved at 1000 °C. X-ray photoelectron spectroscopy and Ultraviolet–Visible diffuse reflectance spectroscopy analyses revealed that high-temperature calcination induced the formation of oxygen vacancies and Ti^{3+} defects, leading to a narrowing of the optical bandgap from 3.01 eV to 2.98 eV. An optimal aging time of 4 h yielded uniform nanoparticles with a high specific surface area, whereas prolonged aging (>6 h) resulted in the re-emergence of $BaCO_3$ impurities and severe agglomeration due to the formation of a rigid gel network. This work provides a precise processing window for fabricating high-purity, highly tetragonal $BaTiO_3$ nanopowders suitable for the next generation of miniaturized electronic devices.

Keywords: barium titanate; sol-gel synthesis; tetragonality; oxygen vacancies; microstructure

Check for updates

Academic Editor: Dmitri Donetski

Received: 4 January 2026
Revised: 21 January 2026
Accepted: 23 January 2026
Published: 30 January 2026

Copyright: © 2026 by the authors. Licensee MDPI, Basel, Switzerland. This article is an open access article distributed under the terms and conditions of the Creative Commons Attribution (CC BY) license.

1. Introduction

Barium titanate ($BaTiO_3$) crystallizes in the prototypical ABO_3 perovskite structure and has held a pivotal position in the field of electronic ceramics since its discovery in the 1940s [1]. Due to its superior dielectric permittivity, ferroelectricity, and positive temperature coefficient of resistivity (PTCR) behavior, $BaTiO_3$ is indispensable in applications such as multilayer ceramic capacitors (MLCCs), PTC thermistors, piezoelectric transducers, memory devices, and optical components [2,3]. The rapid trend toward miniaturization, integration, and high performance in electronic devices has imposed stringent requirements on the dimensions and quality of electronic components. For $BaTiO_3$, the core dielectric material in MLCCs, characteristics such as grain size, distribution, and phase purity directly dictate device performance and reliability [4–7].

To meet miniaturization demands, the dielectric layer thickness in MLCCs has been reduced to 1 μm or less. This necessitates a ceramic grain size below 200 nm to accommodate the minimum requirement of five grains per layer for reliability, while simultaneously maintaining a tetragonality exceeding 1.0080 [8,9]. Traditional solid-state reaction methods, which utilize $BaCO_3$ and TiO_2 precursors reacting at temperatures above 1000 °C [10], offer cost-effective and simple processing suitable for large-scale production. Nevertheless, products obtained via this technique are typically characterized by extensive agglomeration, lack of chemical uniformity, and coarse granularity, rendering them unsuitable for next-generation miniaturized devices [11]. Consequently, various wet chemical techniques have been proposed, including hydrothermal synthesis [12], microwave-assisted synthesis [13], oxalate-based synthesis [14], coprecipitation [15], microemulsion synthesis [16], and sol–gel synthesis [17–19]. Among these, the sol–gel route demonstrates significant merits for synthesizing nanoscale $BaTiO_3$ [20]. This approach employs metal alkoxides or inorganic salts as precursors to form a sol through hydrolysis and condensation [21]. Recent research has demonstrated the versatility of functionalized $BaTiO_3$ for diverse applications, particularly in photocatalysis. For instance, Kaptagay et al. reported that rhodium (Rh) doping significantly modulates the optical properties and enhances the photocatalytic activity of $BaTiO_3$ [22]. Similarly, Ivanov et al. explored the physicochemical properties of $BaTiO_3$/CuO nanocomposites, highlighting their potential under visible and UV light irradiation [23]. On the other hand, recent studies have introduced innovative strategies to overcome the size-effect-induced suppression of tetragonality. For instance, Mohamed-Noriega et al. developed a water-free solvothermal approach using methanol, demonstrating that eliminating the aqueous environment significantly minimizes lattice hydroxyl defects and promotes tetragonality [24]. In parallel, Liu et al. explored thermal processing effects, reporting that fast heating rates favor the formation of the tetragonal phase in sol–gel-derived thin films [25].

Distinct from recent approaches that rely on extrinsic modifications, in this study, $BaTiO_3$ nanopowders are prepared via the sol–gel route, which has the potential to achieve high purity and compositional homogeneity. Distinct from previous studies that focus on single-variable optimization, this work aims to establish a coupled process–structure–defect–property relationship, systematically investigate how the aging time regulates the precursor gel network and carbonate evolution, and how the calcination temperature dictates the phase transition (tetragonality), oxygen vacancy concentration, and bandgap narrowing. This provides a comprehensive physical picture for the controllable synthesis of high-quality $BaTiO_3$.

2. Materials and Methods

2.1. Chemicals and Reagents

The starting materials used in this study included butyl titanate ($Ti(OC_4H_9)_4$, 98%), barium acetate ($(CH3COO)_2Ba$, 99%), and PEG-2000, all purchased from McLean Biochemical Technology Co., Ltd. (Shanghai, China). Acetic acid (CH_3COOH, 99.5%) was supplied by Kemiou Chemical Reagent Co., Ltd. (Tianjin, China), while anhydrous ethanol (CH_3CH_2OH, 99.7%) was acquired from Sinopharm Chemical Reagent Co., Ltd. (Shanghai, China). These analytically pure reagents were utilized as received.

2.2. Preparation Method

First, 0.02 mol of butyl titanate was added to 40 mL of ethanol and stirred at 600 rpm for 0.5 h. Separately, 0.02 mol of barium acetate was dissolved in 20 mL of glacial acetic acid under the same stirring conditions. The barium acetate solution was then added dropwise to the butyl titanate solution under constant stirring at room temperature. To induce

hydrolysis, 9 mL of deionized water was introduced into the mixture. Subsequently, 1 wt% PEG-2000 was incorporated, and stirring was continued for another hour. The reaction mixture was aged in a water bath for various durations (2, 4, 6, 8, and 10 h) to facilitate the gelation process. Drying of the precursor gels was carried out in a vacuum oven at 100 °C for 12 h, ground into fine powders, and calcined at temperatures ranging from 600 to 1000 °C within 3 h of hold time. The calcination was performed in air (uncovered crucibles) with a heating rate of 5 °C/min and a natural cooling rate. Finally, the calcined powders were redispersed in ethanol at a ratio of 1:100, sonicated for 30 min, and dried in an oven at 100 °C for 6 h to obtain the final barium titanate samples for characterization. The primary process parameters of the samples are shown in Table 1.

Table 1. Primary process parameters of the samples.

Sample	Aging Time (h)	Calcination Temperature (°C)	Hold Time (h)
A1	4	600	3
A2	4	700	3
A3	4	800	3
A4	4	900	3
A5	4	1000	3
B1	2	700	3
B2	4	700	3
B3	6	700	3
B4	8	700	3
B5	10	700	3

2.3. Characterization

The crystal structure and phase purity of the samples were determined by X-ray diffraction (XRD, D8 Advance, Bruker, Karlsruhe, Germany) with a Cu-Kα radiation source at a scanning rate of 8°/min. The XRD patterns were collected in the 2θ range of 5–80° with a step size of 0.02° and a counting time of 1 s. Chemical bonding and structural characteristics were investigated using Fourier transform infrared spectroscopy (FT-IR, VERTEX 80, Bruker Optik GmbH, Ettlingen, Germany) and laser confocal Raman spectroscopy (Thermo Scientific DXR, Thermo Fisher Scientific, Madison, WI, USA). The surface morphology and microstructure of the barium titanate were examined via field emission scanning electron microscopy (SEM, JSM-7500F, JEOL Ltd., Tokyo, Japan) and transmission electron microscope (TEM, TALOS-F200X, Thermo Fisher Scientific, Waltham, MA, USA), while the surface composition and valence states were characterized by X-ray photoelectron spectroscopy (XPS, AXIS Supra, Kratos Analytical Ltd., Manchester, UK). Thermal behavior, including mass changes and thermal effects, was evaluated using a simultaneous thermal analyzer (STA 449 F5, NETZSCH-Gerätebau GmbH, Selb, Germany) to generate TG-DSC curves. Additionally, UV–visible diffuse reflectance spectroscopy was recorded on a UV-2600i spectrophotometer (Shimadzu Corporation, Kyoto, Japan). Finally, the specific surface area and pore size distribution were derived from adsorption/desorption isotherms measured using a BELSORP-max fully automated gas adsorption analyzer (MicrotracBEL Corp., Osaka, Japan).

3. Results and Discussion

3.1. TG-DSC Analysis for Precursor

Figure 1 illustrates the thermogravimetric and differential scanning calorimetry (TG-DSC) analysis of the barium titanate dry gel across a temperature range of 30 °C to 1000 °C. The TGA profile reveals a total weight loss of 40%, indicating that three clearly defined

stages are observed during the thermal decomposition of the precursor. The first stage, spanning 30–259 °C, exhibits a weight loss of approximately 13.7%, which is primarily attributed to the evaporation of residual solvents within the gel network [16]. With a total mass reduction of approximately 20%, the second decomposition stage takes place in the interval of 259–513 °C. This phase coincides with two exothermic peaks at 343 °C and 483 °C on the DSC curve. Specifically, the peak at 343 °C is ascribed to the decomposition of titanium acetate into TiO_2 and acetic anhydride, while the peak at 483 °C corresponds to the decomposition of barium acetate into barium carbonate and other pyrolysis products [26]. The third stage is taken place in the range of 720–770 °C, accompanied by a weight loss of 6.4%. The distinct exothermic peak at 740 °C observed in this region could be the reaction between barium carbonate and titanium dioxide, which results in the generation of the barium titanate phase and the release of carbon dioxide [27].

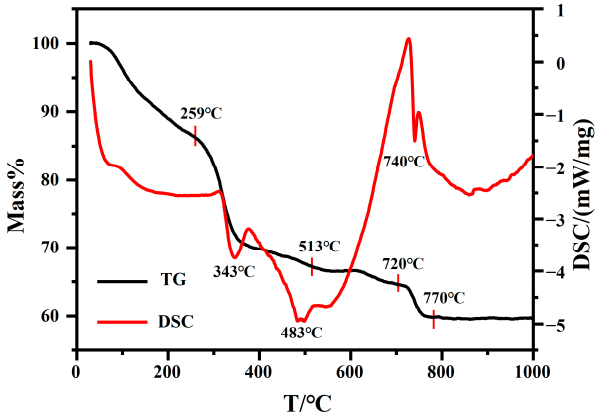


Figure 1. TG-DSC curve of the precursor gel powder. The black curve represents the TG profile (weight loss), and the red curve denotes the DSC profile (heat flow).

3.2. Effect of Calcination Temperature on Nano-$BaTiO_3$ Powder

The XRD patterns of $BaTiO_3$ samples obtained at different calcination temperatures are shown in Figure 2. The minor impurity peaks at 24°, 34°, 43°, and 46° are exhibited in the A1 sample calcined at 600 °C, which can be indexed to $BaCO_3$. This means that at 600 °C, the precursor decomposition was incomplete, preventing the full removal of organic moieties from the gel. Additionally, trace $BaCO_3$ could be formed due to the reaction between the gel and atmospheric CO_2. With increasing calcination temperature, these impurity peaks disappear, while the strengthening of the characteristic $BaTiO_3$ peaks increases, suggesting improved crystallinity.

The distinction between the cubic and tetragonal phases of $BaTiO_3$ is primarily identified by the splitting of the diffraction peak near $2\theta \approx 45°$. For samples calcined between 600 and 800 °C, the (200) reflection appears as a single peak, indicating that $BaTiO_3$ exists in the cubic phase. At 900 °C (Sample A4), as shown in Figure 2b, the peak at $2\theta \approx 45°$ had been broadened and the signs of splitting had occurred, signaling an increase in tetragonal character for $BaTiO_3$ nanoparticles [28–30]. Upon reaching 1000 °C, the A5 sample exhibits a distinct splitting into (002) and (200) peaks. This pattern is well-correlated with the standard tetragonal $BaTiO_3$ card (PDF#89-1428), confirming the formation of the P4mm (99) space group. The average crystallite sizes were calculated using the Scherrer formula, while the c/a ratio, which serves as a critical indicator of tetragonality, was determined via XRD refinement, as shown in Table 2. According to the literature [31], a c/a ratio exceeding 1.0087 denotes a fully developed tetragonal phase. As indicated in Table 2, a c/a ratio of 1.0100 was achieved in sample A5, confirming that a dominant tetragonal phase was obtained at 1000 °C.

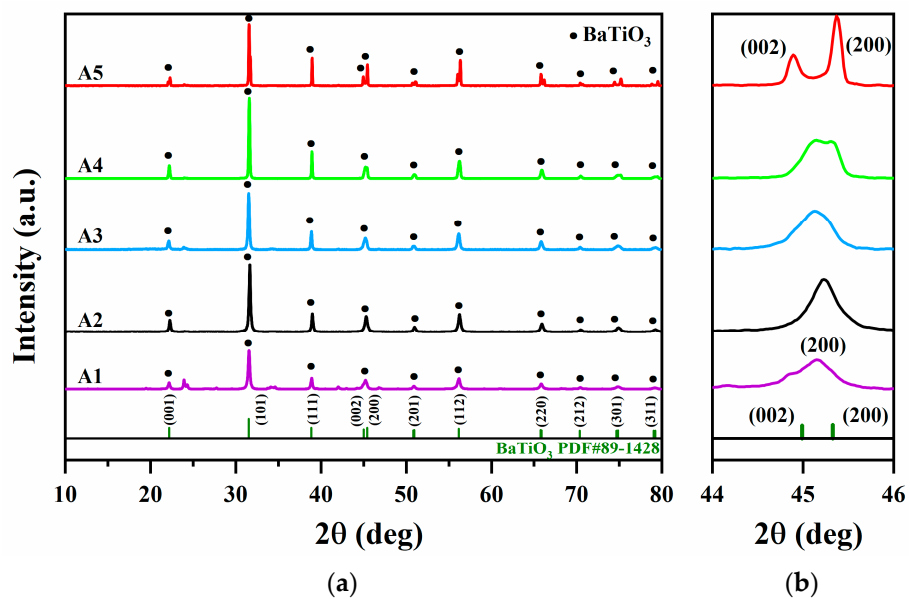


Figure 2. (**a**) XRD patterns of $BaTiO_3$ samples A1–A5, calcined at 600, 700, 800, 900, and 1000 °C, respectively. (**b**) XRD data for the (200) reflection of the prepared $BaTiO_3$.

Table 2. The summary of the grain size and the lattice parameters of nano-$BaTiO_3$ under different calcining temperatures.

Sample	Calcination Temperature (°C)	Size (nm)	c/a
A1	600	32.1	1.0000
A2	700	35.5	1.0020
A3	800	40.8	1.0042
A4	900	65.5	1.0047
A5	1000	>100	1.0100

To further evaluate the quality of the synthesized powders, these values were compared with standard commercial products. Commercial hydrothermal $BaTiO_3$ powders typically exhibit a fine particle size (100 nm) but a relatively lower tetragonality ($c/a \approx 1.008$) due to the entrapped hydroxyl defects. On the other hand, commercial solid-state powders possess high tetragonality ($c/a > 1.010$) but generally suffer from coarser particle sizes (200–500 nm) and broader size distributions. The $BaTiO_3$ powders prepared in this study exhibit high tetragonality while simultaneously possessing a significantly finer particle size, demonstrating promising application prospects in the field of electronic ceramics.

To identify the functional groups and chemical bonds, the samples were examined by FT-IR spectroscopy. As presented in Figure 3a, five distinct characteristic absorption bands are observable in the spectra of samples calcined at various temperatures. According to the relevant literature [32], the absorption band near 3437 cm^{-1} is ascribed to the vibrations of the O-H groups that have been adsorbed from the air. The bands at 1443 cm^{-1} and 854 cm^{-1} correspond to the stretching and deformation vibrations of the carbonate group (CO_3^{2-}) in $BaCO_3$ [33], respectively. Meanwhile, the bands at 450 cm^{-1} and 594 cm^{-1} represent the deformation and stretching vibrations of Ti-O bonds within the TiO_6 octahedra, serving as the primary characteristic fingerprints of $BaTiO_3$ [33]. Notably, the CO_3^{2-} absorption band at 1443 cm^{-1} is significantly more intense in the sample A1, indicating a higher $BaCO_3$ content, which has been corroborated by the XRD results.

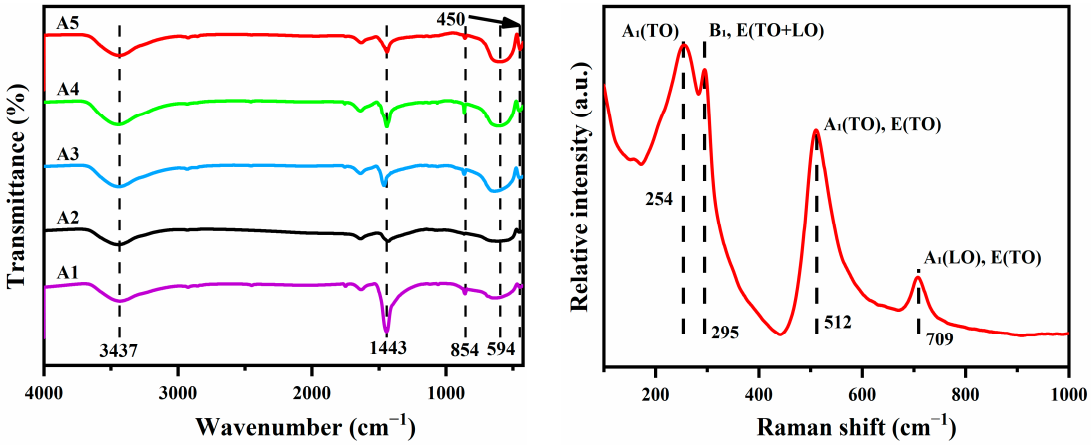


Figure 3. (**a**) FT-IR spectra of $BaTiO_3$ samples A1–A5, calcined at 600, 700, 800, 900, and 1000 °C, respectively. (**b**) Raman spectra of the A5 (1000 °C) sample.

To definitively confirm the formation of tetragonal $BaTiO_3$ nanoparticles, sample A5 was characterized by Raman spectroscopy, as shown in Figure 3b. Tetragonal $BaTiO_3$ belongs to the P4mm space group, which possesses characteristic Raman-active optical phonon modes defined as $3A_1 + 4E + B_1$ [34]. As illustrated in Figure 3b, the sample exhibits distinct Raman peaks at 254 cm^{-1}, 295 cm^{-1}, 512 cm^{-1}, and 709 cm^{-1} [35]. Specifically, the sharp peaks at 295 cm^{-1} (assigned to E(TO + LO)) and 709 cm^{-1} (assigned to A_1(LO)) are intrinsic features of the tetragonal phase. The presence of these specific modes in the Raman spectrum confirms that pure tetragonal $BaTiO_3$ is successfully obtained after calcination at 1000 °C for 3 h.

The morphology and microstructure of the synthesized samples were characterized using scanning electron microscopy (SEM). The nano-$BaTiO_3$ with controllable particle sizes was successfully synthesized by precisely regulating the calcination temperature as shown in Figure 4. The larger particle size observed in SEM compared to the crystallite size from XRD indicates that the particles are polycrystalline or agglomerated. As depicted in Figure 4a, for the sample calcined at 600 °C, a broad particle size distribution is observed, which could be the presence of barium carbonate in the previous XRD and FT-IR findings, which can likely be attributed to the larger dimensions of $BaCO_3$ particles compared to those of $BaTiO_3$. Meanwhile, extensive and loose flocculent agglomerates were observed, indicating that while $BaTiO_3$ crystallization had been initiated, the process was incomplete, thereby limiting particle growth. An average particle size of approximately 57.28 nm has been revealed using statistical analysis, and a broad unimodal peak is displayed within the distribution curve. Upon increasing the temperature to 700 °C and 800 °C, the $BaCO_3$ phase is eliminated, and the particle size is increased, with the samples existing primarily in the cubic phase. At 900 °C, the particle size had been further enlarged to an average of 81.59 nm; this change could be coincided with the phase transition from cubic to tetragonal. When the temperature reaches 1000 °C, the particle size increases significantly to 140.05 nm. Large, angular and block-like crystals are observed in the sample, suggesting that driven by grain boundary migration, smaller agglomerated grains had coalesced and grown into larger and well-defined crystals. At this stage, the transformation of the tetragonal phase is complete. In summary, both the grain size and crystal phase of $BaTiO_3$ could be effectively modulated by adjusting the calcination temperature.

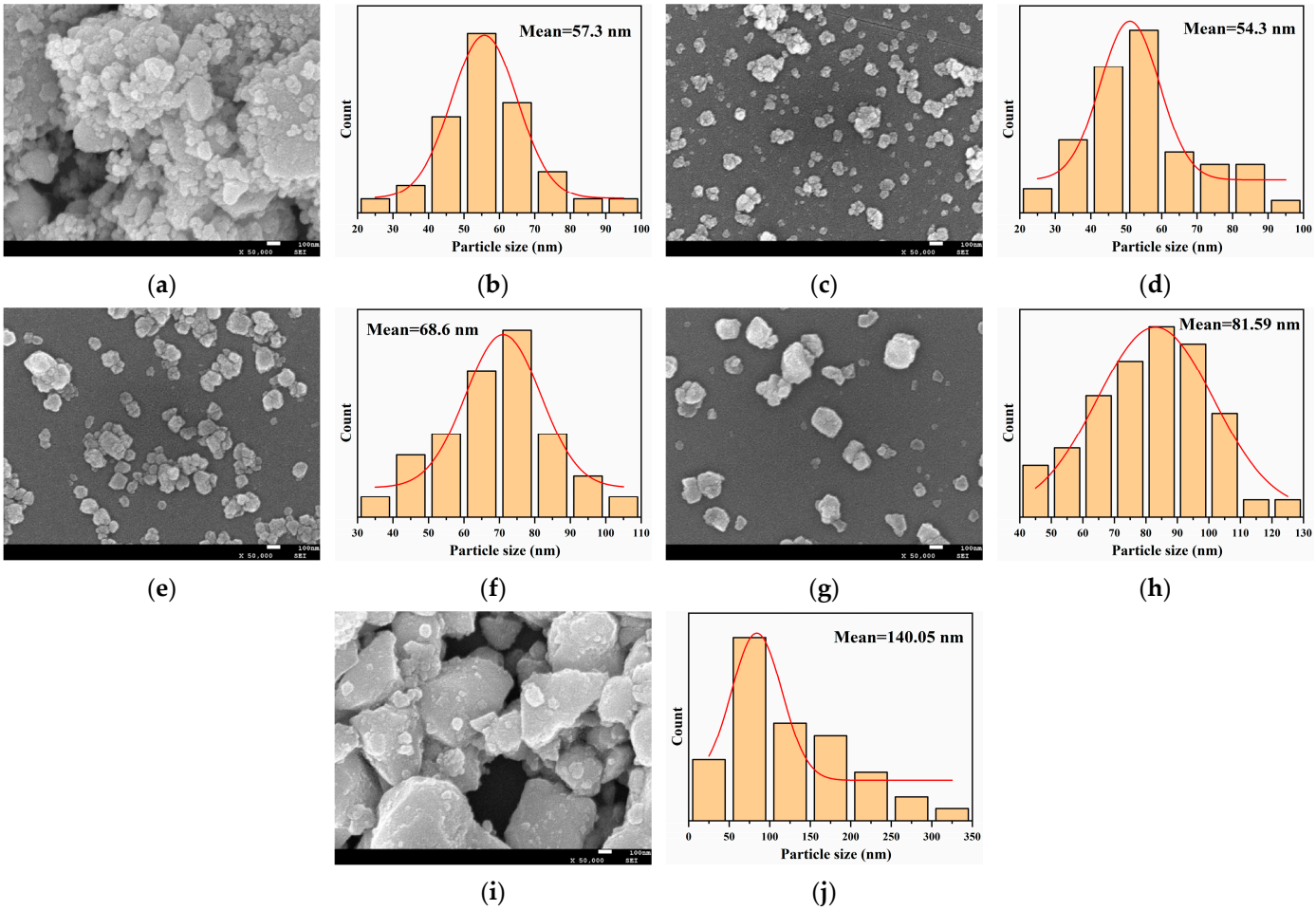


Figure 4. SEM micrographs and particle size distribution of (**a**,**b**) sample A1, (**c**,**d**) sample A2, (**e**,**f**) sample A3, (**g**,**h**) sample A4, and (**i**,**j**) sample A5.

To further elucidate the microstructural evolution and phase transformation of the synthesized powders, the transmission electron microscopy (TEM) and high-resolution TEM (HRTEM) were conducted on samples A1 to A5 and calcined at different temperatures. Sample A1, calcined at 600 °C, is characterized by small, agglomerated particles with irregular boundaries, indicative of an incipient stage of crystallization. In contrast, sample A5, calcined at 1000 °C, reveals significantly larger, well-defined grains with distinct edges, which is well-correlated with the SEM observations.

Well-developed lattice fringes for (110) or (111) crystal planes are clearly observed at particles of samples A1, A2, A3, A4, and A5, respectively. Sample A1 exhibits an interplanar spacing of 0.236 nm, as shown in Figure 5b, which is indexed to the (111) plane of $BaTiO_3$. The relatively indistinct lattice fringes in this sample suggest lower crystallinity or the presence of amorphous domains. Conversely, sample A5 displays clearly continuous lattice fringes with a measured d-spacing of 0.283 nm, as shown in Figure 5j, corresponding to the (110) plane of $BaTiO_3$. Furthermore, the selected area electron diffraction (SAED) is conducted on sample A5, as shown in Figure 5k. The sharp and discrete diffraction spots are observed in the pattern of sample A5, which confirms its single-crystalline nature and could be indexed as a tetragonal structure.

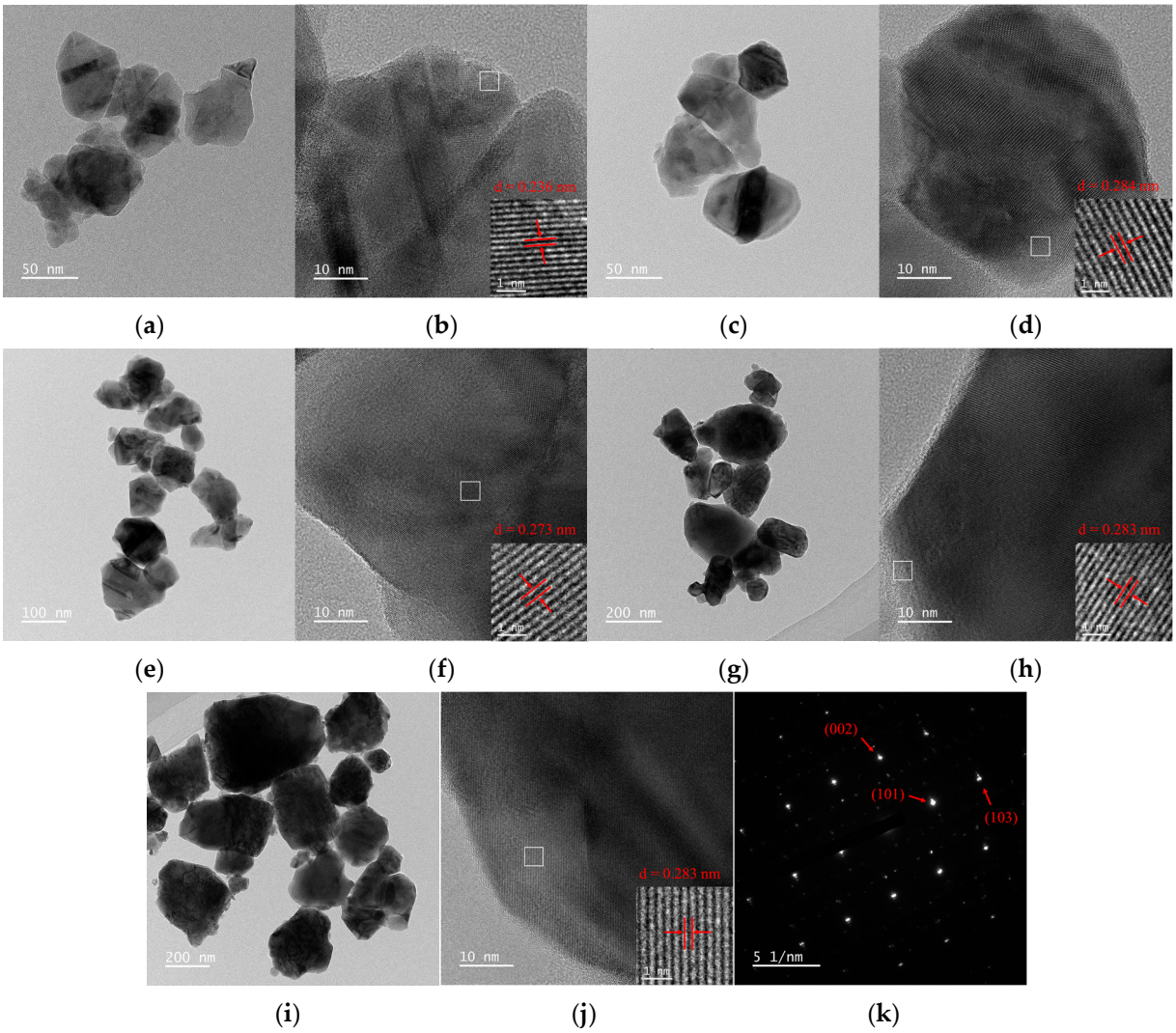


Figure 5. TEM image and HRTEM image of (**a**,**b**) sample A1, (**c**,**d**) sample A2, (**e**,**f**) sample A3, (**g**,**h**) sample A4, (**i**,**j**) sample A5, and (**k**) SAED pattern of sample A5.

The elemental composition and chemical states of samples A3, A4, and A5 were investigated using XPS. The presence of Ba, Ti, C, and O had been confirmed in the XPS survey spectrum as shown in Figure 6a, verifying the successful preparation of nano-$BaTiO_3$ powder. Figure 6b presents the high-resolution Ba 3d XPS spectrum. Two distinct peaks located at 777.71 eV and 792.74 eV are attributed to the Ba $3d_{5/2}$ and Ba $3d_{3/2}$ spin–orbit doublets, respectively. The binding energies agree with the Ba^{2+} oxidation state in the perovskite lattice [36]. Figure 6c displays the high-resolution Ti 2p spectrum, which can be fitted into two distinct oxidation states. The dominant peaks at 458.16 eV (Ti $2p_{3/2}$) and 463.89 eV (Ti $2p_{1/2}$) are attributed to Ti^{4+} ions in the octahedral coordination of the $BaTiO_3$ lattice. Conversely, the peaks at 456.09 eV (Ti $2p_{3/2}$) and 461.77 eV (Ti $2p_{1/2}$) correspond to Ti^{3+} species [37–39]. The high-resolution O 1s XPS spectra (Figure 6d) display a peak at 528.68 eV, assigned to the lattice oxygen (O^{2-}) in the $BaTiO_3$ structure. The peak located at 531.75 eV is generally attributed to non-lattice oxygen. This higher binding energy component (531.75 eV) represents a collective contribution from both intrinsic oxygen vacancy regions and extrinsic surface species, such as hydroxyl groups (-OH) and adsorbed oxygen, which are inevitable in sol–gel-derived nanopowders. The presence of Ti^{3+} is intrinsically linked to the formation of oxygen vacancies. During high-temperature sintering, lattice oxygen is released into the environment (Equation (1)), creating oxygen

vacancies and free electrons. To maintain charge neutrality, Ti^{4+} ions capture these electrons and are reduced to Ti^{3+} (Equation (2)). Notably, with the rise in calcination temperature, the intensity of the Ti^{3+} peaks rises. This trend suggests that higher temperatures promote the release of lattice oxygen, thereby generating a higher concentration of oxygen vacancies and Ti^{3+} defects.

$$O_O^X \leftrightarrow \frac{1}{2}O_2 + V_{\ddot{O}} + 2e^- \quad (1)$$

$$Ti^{4+} + e^- \leftrightarrow Ti^{3+} \quad (2)$$

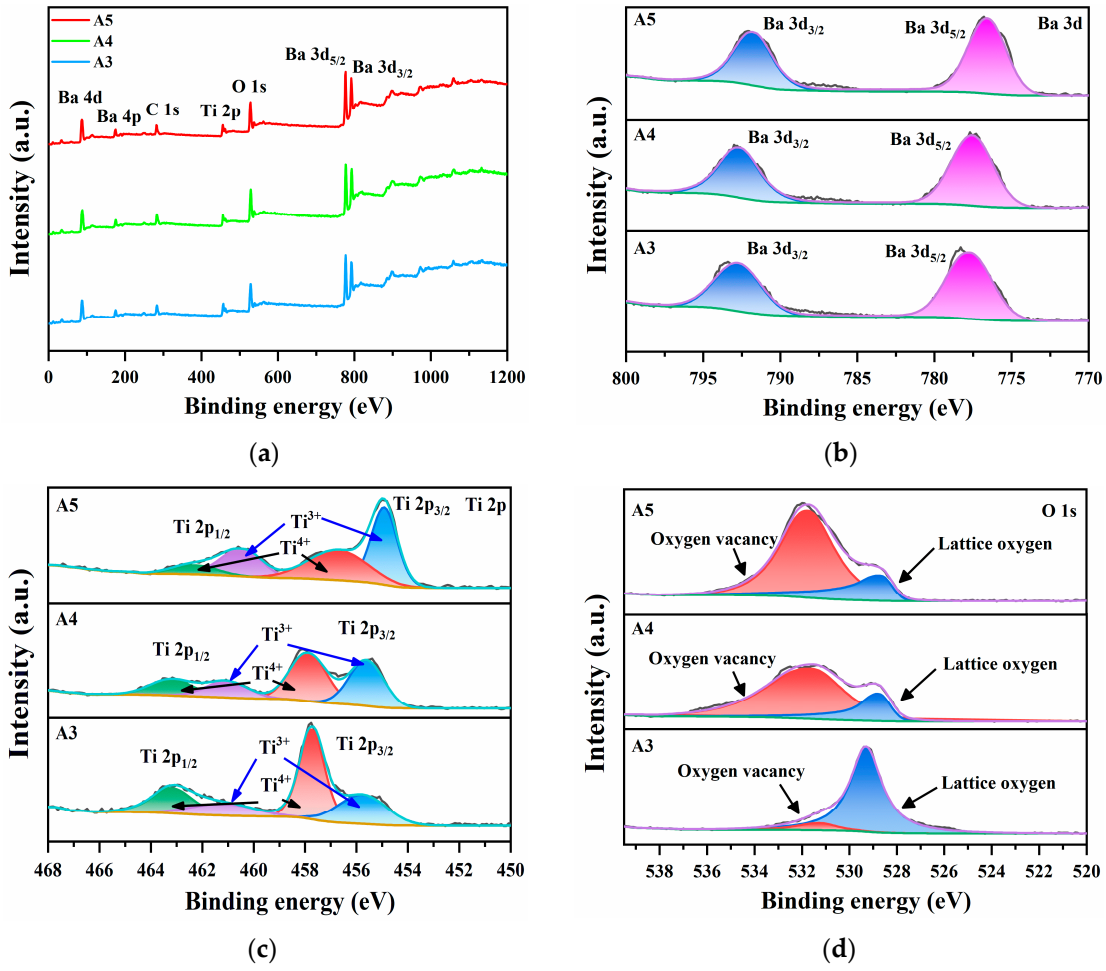


Figure 6. (**a**) XPS full spectrum of A3, A4, and A5 samples; (**b**) high-resolution spectra of Ba 3d of A3, A4, and A5 samples; (**c**) high-resolution spectra of Ti 2p of A3, A4, and A5 samples; (**d**) high-resolution spectra of O 1s of A3, A4, and A5 samples.

The diffuse reflectance properties were investigated using UV–Vis diffuse reflectance spectroscopy (DRS), as shown in Figure 7a. For sample preparation, the powders were mixed with $BaSO_4$ as a reference and pressed into a holder for measurement. It is revealed that the absorption edge of the $BaTiO_3$ synthesized at 1000 °C exhibits a distinct red shift toward the visible region. The bandgap energy (Eg) was estimated using the Tauc method based on the K-M function [40].

$$F(R) = \frac{(1-R)^2}{2R} = \frac{K}{S} \quad (3)$$

$$(F(R)h\nu)^{\frac{1}{n}} = B(h\nu - Eg) \quad (4)$$

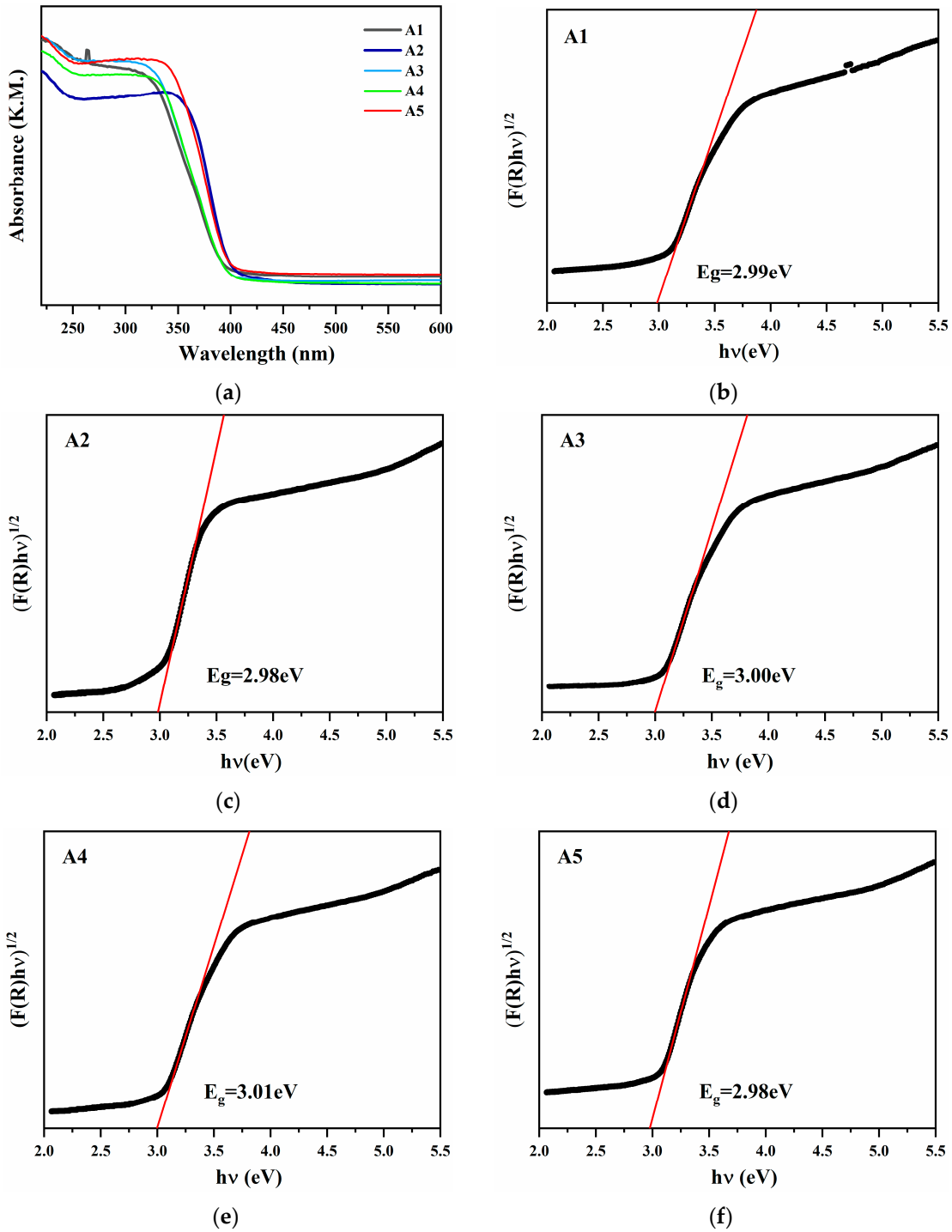


Figure 7. (**a**) UV–Vis DRS spectra of A1–A5 samples, calcined at 600, 700, 800, 900, and 1000 °C; (**b**–**f**) forbidden bandgap of A1–A5 samples.

In the equation, h is Planck's constant; ν is the frequency of light; Eg is the bandgap; R is the reflectance (expressed as a percentage); K is the absorption coefficient; S is the reflectance coefficient; B is the proportionality constant; and n is determined by the type of electronic transition, being 2 for indirect bandgap semiconductors and 1/2 for direct bandgap semiconductors. $BaTiO_3$ is an indirect bandgap semiconductor, so $n = 2$. The bandgap was determined by plotting $(F(R)h\nu)^{1/2}$ against the photon energy ($h\nu$) and extrapolating the linear portion of the curve to the x-axis. The resulting Tauc plots are presented in Figure 7b–d. The calculated Eg values for samples calcined at 600 °C, 700 °C, 800 °C, 900 °C, and 1000 °C are 2.99 eV, 2.98 eV, 3.00 eV, 3.01 eV, and 2.98 eV, respectively.

Theoretically, the enhanced crystallinity associated with higher calcination temperatures (e.g., 1000 °C) is typically expected to widen the bandgap. However, the anomalous bandgap at 600 °C is likely associated with the size effect, in conjunction with influences from incomplete crystallization and residual carbonaceous impurities. And the observed narrowing of the bandgap to 2.98 eV at 1000 °C contradicts this trend. Based on the XPS analysis discussed previously, this phenomenon is attributed to the increased concentration of oxygen vacancies formed at high temperature. These vacancies introduce localized donor states below the conduction band, effectively causing a red shift in the absorption edge and a consequent reduction in the optical bandgap.

3.3. Effect of Aging Time on Nano-$BaTiO_3$ Powder

The crystal structure evolution of $BaTiO_3$ synthesized at different aging times (2 h, 4 h, 6 h, 8 h and 10 h) was investigated via XRD. As depicted in Figure 8, diffraction peaks located at 22.2°, 31.6°, 38.9°, 45.2°, 56.2°, 65.9°, and 74.9° align well with the standard cubic $BaTiO_3$ pattern (PDF#79-2263), confirming the formation of the Pm-3m space group. Notably, when the aging time extends to 6 h, the diffraction peaks associated with barium carbonate impurities are intensified significantly. It is attributed to the prolonged exposure to atmospheric CO_2, which is dissolved to form carbonate ions (CO_3^{2-}), thereby facilitating the precipitation of $BaCO_3$. However, upon aging for 10 h, the intensity of the $BaCO_3$ peaks diminish, indicating a reduction in impurity content. This phenomenon is plausibly ascribed to the enhanced densification and stability of the gel network at this stage. The consequent shrinkage and closure of pores create a compact barrier that effectively hinders the diffusion of external CO_2 into the gel interior, thereby mitigating further carbonation. Grain sizes calculated using the Scherrer formula during varied aging times for B1, B2, B3, B4, and B5 were determined to be 41.7 nm, 35.5 nm, 40.1 nm, 44.2 nm, and 47.4 nm, respectively.

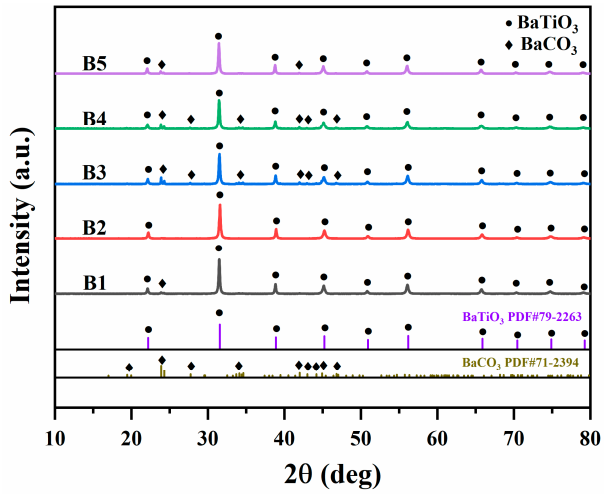


Figure 8. XRD patterns of $BaTiO_3$ samples B1–B5 obtained with aging times of 2, 4, 6, 8, and 10 h.

The non-monotonic evolution of the $BaCO_3$ phase can be elucidated by the competition between hydrolysis and polycondensation during aging. Initially (0–6 h), the hydrolysis of alkoxides prevails, forming a loose and open gel network. This structure facilitates the diffusion of atmospheric CO_2 and its reaction with active Ba^{2+}, leading to an increase in $BaCO_3$ content [41]. However, with prolonged aging (up to 10 h), polycondensation reactions become dominant. According to Brinker and Scherer [21], this stage is characterized by the spontaneous shrinkage and stiffening of the gel network. This process significantly densifies the gel skeleton and reduces porosity, thereby acting as a physical barrier that restricts CO_2 diffusion [42].

To identify the functional groups and chemical bonds, the samples were examined by FT-IR spectroscopy. As illustrated in Figure 9, three distinct characteristic absorption bands are discernible in the infrared spectra of samples aged for different durations. According to the relevant literature, the absorption bands at 1443 cm^{-1} and 854 cm^{-1} are assigned to the stretching and deformation vibrations of the carbonate group (CO_3^{2-}) in $BaCO_3$, respectively. Meanwhile, the band at 605 cm^{-1} corresponds to the stretching vibration of Ti-O bonds within TiO_6 octahedra, which serves as a primary characteristic fingerprint of $BaTiO_3$. As depicted in Figure 9, sample B3 exhibits a significantly more intense carbonate absorption band at 1443 cm^{-1} compared to sample B5, indicating a higher concentration of $BaCO_3$ impurities in B3. This observation corroborates the findings from the XRD analysis.

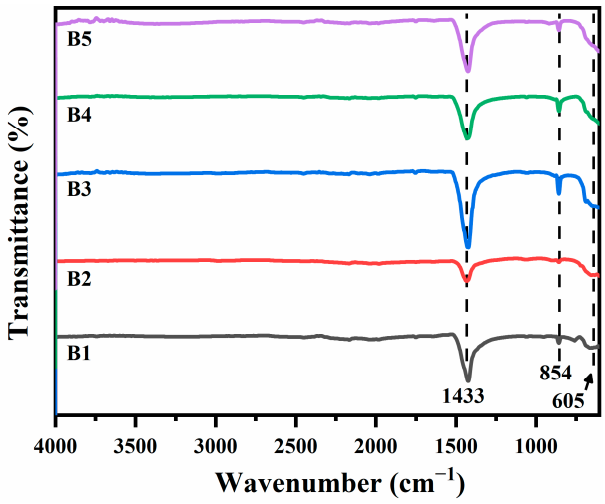


Figure 9. FT-IR spectra of $BaTiO_3$ samples B1–B5 obtained with aging times of 2, 4, 6, 8, and 10 h.

Scanning electron microscopy (SEM) was employed to characterize the morphology and microstructure of the samples, as illustrated in Figure 10. For the sample aged for 2 h, severe agglomeration resulted in an irregular morphology, where numerous fine primary particles are sintered into hard agglomerates. It is likely attributed to compositional inhomogeneity in the precursor and the vigorous decomposition of organic components. Conversely, at 4 h of aging, a uniform gel composition and complete gelation had been achieved from the precursor, yielding nanoparticles with uniform size and excellent dispersibility after heat treatment. However, upon extending the aging time to 6 h, the onset of particle agglomeration was observed. With a further increase to 8–10 h, severe agglomeration had been re-emerged. This degradation is ascribed to the excessive rigidity and density of the gel network caused by prolonged aging, which facilitates sintering and agglomeration during the subsequent high-temperature treatment. It is confirmed that varying the aging time had a negligible influence on the grain size but significantly impacted the dispersion of the particles.

The elemental composition and chemical states of samples B1, B3, and B5 were investigated using XPS. The presence of Ba, Ti, C, and O had been confirmed in the XPS survey spectrum as shown in Figure 11a, verifying the successful synthesis of nano-$BaTiO_3$ powder. Figure 11b illustrates the high-resolution Ba 3d spectrum. The peaks observed at 777.80 eV and 792.70 eV are attributed to the Ba $3d_{5/2}$ and Ba $3d_{3/2}$ spin–orbit split components, respectively, confirming the presence of the Ba^{2+} oxidation state. Figure 11c displays the high-resolution Ti 2p spectrum, where the peaks at 462.51 eV and 464.44 eV are attributed to the Ti $2p_{1/2}$ orbital, while those at 458.95 eV and 457.54 eV correspond to the Ti $2p_{3/2}$ orbital. These binding energies are consistent with the typical characteristics of Ti species in an oxide environment. The high-resolution C 1s spectrum is presented in Figure 11d.

The peak at 284.76 eV is assigned to adventitious C-C bonds and functions as the internal standard. The component at 286.95 eV is attributed to C=O species derived from acetate groups. Notably, in sample B3, the peak located at 290.13 eV is ascribed to carbonate species (CO_3^{2-}), signifying the presence of surface barium carbonate. In contrast, sample B5 exhibits a reduced intensity for this carbonate peak, indicating a lower concentration of surface $BaCO_3$. This finding corroborates the results obtained from the preceding XRD and FT-IR analyses.

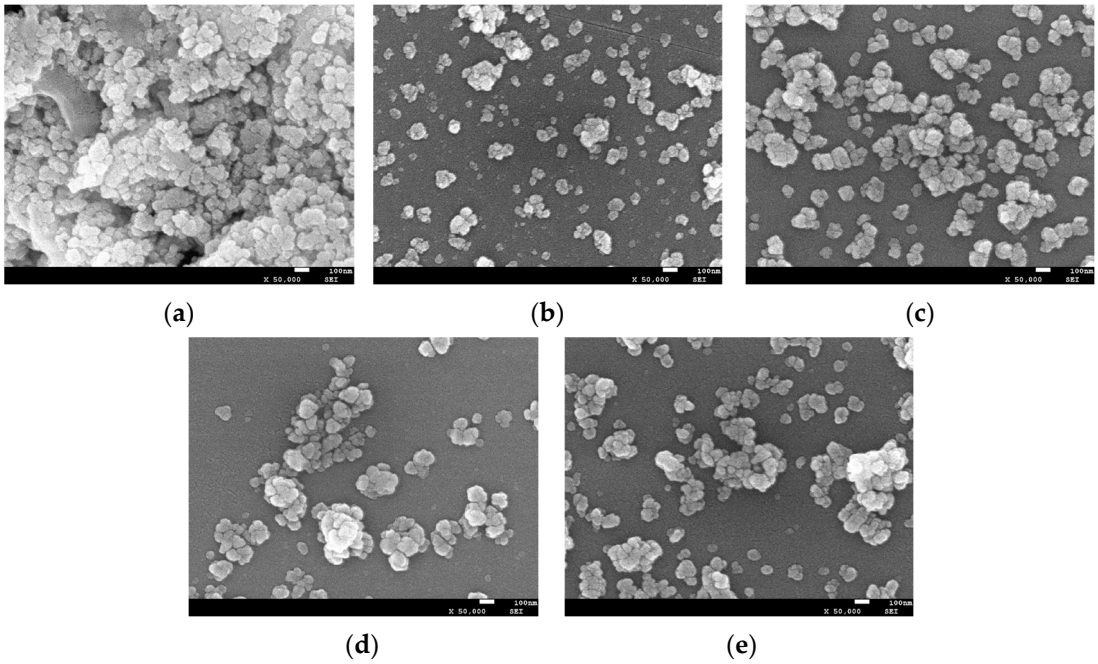


Figure 10. SEM images and particle size distribution of (**a**) sample B1, (**b**) sample B2, (**c**) sample B3, (**d**) sample B4, and (**e**) sample B5.

Nitrogen adsorption–desorption measurements were carried out to calculate the specific surface area and evaluate the pore characteristics of the samples. As illustrated in Figure 12, the *Y*-axis (cm^3 STP/g) represents the volume of gas adsorbed at standard temperature and pressure per gram of sample, while the *X*-axis (P/P_0) represents the relative pressure. All samples exhibit Type III isotherms, which correspond to weak adsorbent–adsorbate interactions. These isotherms are characterized by distinct hysteresis loops, indicative of the presence of flat, slit-like pores. Table in Figure 12a lists the specific surface area (S_{BET}) and pore volume measured by isotherms at different aging times. Significant variations in specific surface area were observed among samples subjected to different aging times, suggesting that the aging process critically influences the sintering activity and grain growth behavior of the final product. Notably, sample B2 (aged for 4 h) displays the highest specific surface area and pore volume. It implies that this sample possesses the smallest grain size, which aligns with the crystallite size of the calculations presented earlier. Furthermore, it is well-established that powders with a high specific surface area possess elevated surface energy, which serves as a thermodynamic driving force, enhancing sintering activity during the subsequent sintering processes of ceramic, thereby facilitating densification at lower temperatures. Although the sample aged for 10 h also exhibits a relatively large specific surface area, excessive aging introduces deleterious $BaCO_3$ impurities and promotes powder agglomeration. As shown in Figure 12b, the *Y*-axis represents the derivative of pore volume with respect to the pore diameter, showing the distribution of pore sizes. The BJH (Barrett–Joyner–Halenda) pore size distribution curves reveal a predominance of pores within the 0–10 nm range. The observed fluctuations in

the distribution curves are attributed to the derivative nature of the BJH method, which inherently amplifies experimental noise. Furthermore, the disordered inter-particle voids formed by the random stacking of $BaTiO_3$ nanoparticles contribute to the complex and broad pore size distribution. Pores of moderate size are favorable for mass transport kinetics, whereas excessively small or large pores may impede effective transport. It is suggested that the optimal aging duration is 4 h, which secures a sufficiently high specific surface area and homogeneity to suppress excessive $BaCO_3$ formation, while avoiding the severe agglomeration associated with prolonged aging.

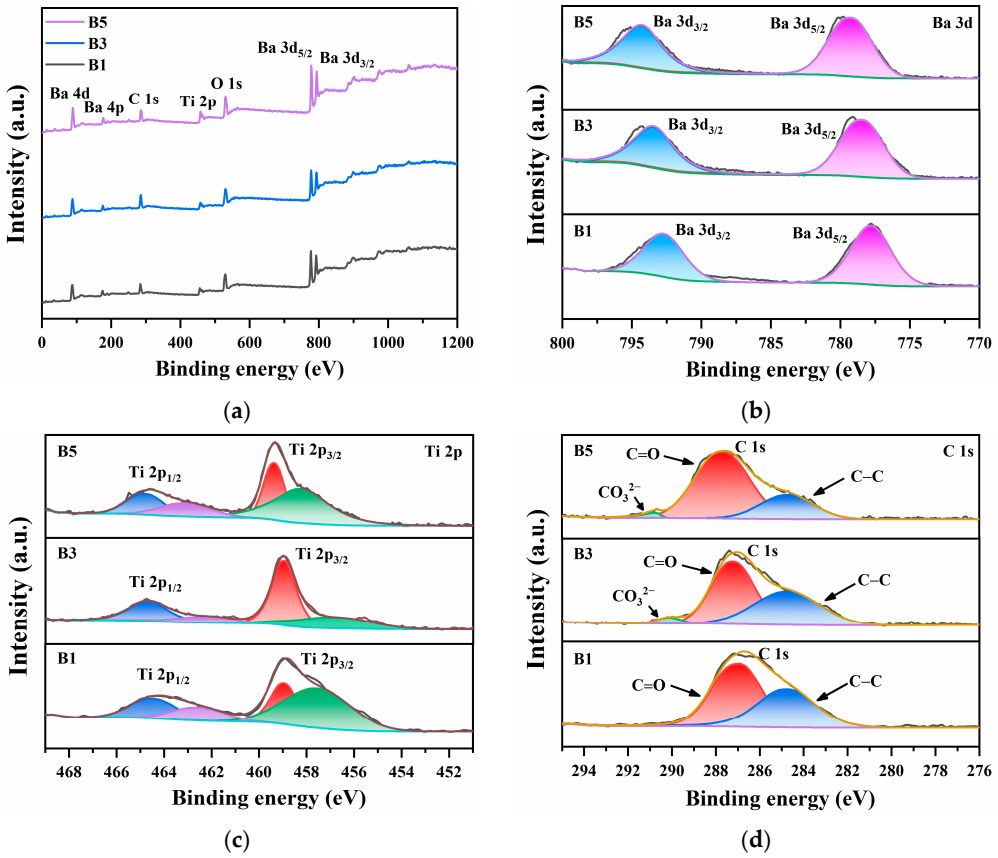


Figure 11. (**a**) XPS full spectrum of B1, B3, and B5 samples; (**b**) high-resolution spectra of Ba 3d of B1, B3, and B5 samples; (**c**) high-resolution spectra of Ti 2p of B1, B3, and B5 samples; and (**d**) high-resolution spectra of C 1s of B1, B3, and B5 samples.

Sample	S_{BET}($m^2 \cdot g^{-1}$)	Pore Volume($cm^3 \cdot g^{-1}$)
B1	6.3912	0.057429
B2	10.373	0.071300
B3	6.4874	0.063822
B4	6.0739	0.066204
B5	8.9731	0.082210

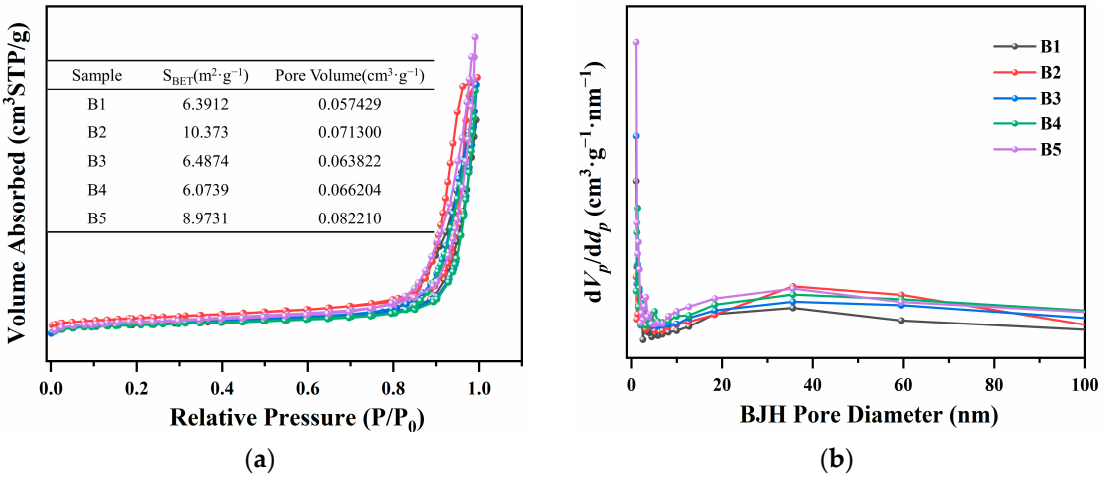


Figure 12. (**a**) N_2 adsorption–desorption isotherms of B1–B5 samples. (**b**) Pore size distribution curves.

4. Conclusions

In this work, nano-sized $BaTiO_3$ powders were successfully prepared via a sol–gel route. The influence of processing parameters on the crystallographic structure, morphology, and defect chemistry was thoroughly analyzed. The crystal structure of $BaTiO_3$ transformed from a cubic phase to a tetragonal phase with increasing calcination temperature. A fully developed tetragonal phase with a c/a ratio of 1.0100 was obtained at 1000 °C, confirming the high quality of the synthesized powder. High-temperature calcination facilitated the release of lattice oxygen, resulting in the generation of oxygen vacancies and the reduction of Ti^{4+} to Ti^{3+}. This defect generation introduced donor states below the conduction band, causing a red shift in the absorption edge and reducing the bandgap energy from 3.01 eV to 2.98 eV. The aging time played a decisive role in determining the homogeneity and purity of the precursors. Shorter aging times (2 h) led to inhomogeneous gels and agglomeration, while excessive aging times (>6 h) caused the rigidity of the gel network to increase and promoted the absorption of atmospheric CO_2, leading to the reformation of $BaCO_3$ impurities. The optimal production of well-dispersed nanoparticles with a size of 35.5 nm were obtained within 4 h at 700 °C, which is minimal agglomeration. In summary, this study demonstrates the simultaneous control of particle dispersion, tetragonality, oxygen-vacancy concentration, and optical bandgap through a dual-tuning strategy involving aging time and calcination temperature. The synthesized $BaTiO_3$ powders with controllable size, high purity, and excellent tetragonality could be potential for the application of electronic ceramics.

Author Contributions: Methodology, S.L.; software, H.-W.L. and H.-X.Z.; writing—original draft, S.L.; writing—review and editing, Y.-H.S. and D.Z.; funding acquisition Y.-H.S.; data curation, S.L. and Y.Y.; investigation, L.L. and X.-P.J.; software, H.-W.L. and H.-X.Z. All authors have read and agreed to the published version of the manuscript.

Funding: This work was supported by the National Key Research and Development Program of China (No. 2023YFB3812200).

Data Availability Statement: The original contributions presented in this study are included in the article. Further inquiries can be directed to the corresponding author.

Conflicts of Interest: The authors declare no conflicts of interest.

References

1. Haertling, G.H. Ferroelectric Ceramics: History and Technology. *J. Am. Ceram. Soc.* **1999**, *82*, 797–818. [CrossRef]
2. Lu, W.; Quilitz, M.; Schmidt, H. Nanoscaled $BaTiO_3$ powders with a large surface area synthesized by precipitation from aqueous solutions:: Preparation, characterization and sintering. *J. Eur. Ceram. Soc.* **2007**, *27*, 3149–3159. [CrossRef]
3. Acosta, M.; Novak, N.; Rojas, V.; Patel, S.; Vaish, R.; Koruza, J.; Rossetti, G.A., Jr.; Rödel, J. $BaTiO_3$-based piezoelectrics: Fundamentals, current status, and perspectives. *Appl. Phys. Rev.* **2017**, *4*, 041305. [CrossRef]
4. Pithan, C.; Hennings, D.; Waser, R. Progress in the Synthesis of Nanocrystalline $BaTiO_3$ Powders for MLCC. *Int. J. Appl. Ceram. Technol.* **2005**, *2*, 1–14. [CrossRef]
5. Hongo, K.; Kurata, S.; Jomphoak, A.; Inada, M.; Hayashi, K.; Maezono, R. Stabilization Mechanism of the Tetragonal Structure in a Hydrothermally Synthesized $BaTiO_3$ Nanocrystal. *Inorg. Chem.* **2018**, *57*, 5413–5419. [CrossRef]
6. Saleem, M.; Butt, M.S.; Maqbool, A.; Umer, M.A.; Shahid, M.; Javaid, F.; Malik, R.A.; Jabbar, H.; Waseem Khalil, H.M.; Hwan, L.D.; et al. Percolation phenomena of dielectric permittivity of a microwave-sintered $BaTiO_3$–Ag nanocomposite for high energy capacitor. *J. Alloys Compd.* **2020**, *822*, 153525. [CrossRef]
7. Özen, M.; Mertens, M.; Snijkers, F.; Cool, P. Hydrothermal synthesis and formation mechanism of tetragonal barium titanate in a highly concentrated alkaline solution. *Ceram. Int.* **2016**, *42*, 10967–10975. [CrossRef]
8. Zhu, C.; Zhao, Q.; Cai, Z.; Guo, L.; Li, L.; Wang, X. High reliable non-reducible ultra-fine $BaTiO_3$-based ceramics fabricated via solid-state method. *J. Alloys Compd.* **2020**, *829*, 154496. [CrossRef]
9. Han, J.-M.; Joung, M.-R.; Kim, J.-S.; Lee, Y.-S.; Nahm, S.; Choi, Y.-K.; Paik, J.-H. Hydrothermal Synthesis of $BaTiO_3$ Nanopowders Using TiO_2 Nanoparticles. *J. Am. Ceram. Soc.* **2014**, *97*, 346–349. [CrossRef]

10. Hsiang, H.-I.; Chang, Y.-L.; Fang, J.-S.; Yen, F.-S. Polyethyleneimine surfactant effect on the formation of nano-sized $BaTiO_3$ powder via a solid state reaction. *J. Alloys Compd.* **2011**, *509*, 7632–7638.
11. Xue, P.; Hu, Y.; Xia, W.; Wu, H.; Zhu, X. Molten-salt synthesis of $BaTiO_3$ powders and their atomic-scale structural characterization. *J. Alloys Compd.* **2017**, *695*, 2870–2877. [CrossRef]
12. Ma, Y.; Vileno, E.; Suib, S.L.; Dutta, P.K. Synthesis of Tetragonal $BaTiO_3$ by Microwave Heating and Conventional Heating. *Chem. Mater.* **1997**, *9*, 3023–3031. [CrossRef]
13. Masuda, Y.; Yamada, T.; Koumoto, K. Synthesis of Acicular $BaTiO_3$ Particles using Acicular Barium Oxalates. *Cryst. Growth Des.* **2008**, *8*, 169–171. [CrossRef]
14. Zhang, X.; Yue, J.; Zhao, Y.; Yan, Z.; Zhu, G.; Liu, L.; Xu, H.; Yu, A. Synthesis of tetragonal $BaTiO_3$ nano-particle via a novel tartaric acid co-precipitation process. *Ceram. Int.* **2021**, *47*, 7263–7267. [CrossRef]
15. Sakabe, Y.; Yamashita, Y.; Yamamoto, H. Dielectric properties of nano-crystalline $BaTiO_3$ synthesized by micro-emulsion method. *J. Eur. Ceram. Soc.* **2005**, *25*, 2739–2742. [CrossRef]
16. Li, W.; Xu, Z.; Chu, R.; Fu, P.; Hao, J. Structure and electrical properties of $BaTiO_3$ prepared by sol–gel process. *J. Alloys Compd.* **2009**, *482*, 137–140. [CrossRef]
17. Hao, Y.; Wang, X.; Zhang, H.; Guo, L.; Li, L. Sol–gel based synthesis of ultrafine tetragonal $BaTiO_3$. *J. Sol-Gel Sci. Technol.* **2013**, *67*, 182–187. [CrossRef]
18. Wu, Y.T.; Wang, X.F.; Yu, C.L.; Li, E.Y. Preparation and Characterization of Barium Titanate ($BaTiO_3$) Nano-Powders by Pechini Sol-Gel Method. *Mater. Manuf. Process.* **2012**, *27*, 1329–1333. [CrossRef]
19. Livage, J.; Henry, M.; Sanchez, C. Sol-gel chemistry of transition metal oxides. *Prog. Solid State Chem.* **1988**, *18*, 259–341. [CrossRef]
20. Jiang, M.; Lu, J.; Chen, Y.; Chen, J.; Cao, X.; Wang, H. Non-hydrolytic sol-gel synthesis of $BaTiO_3$ nano-powder: Effect of calcination temperature and modified titanium source on particles. *Mater. Today Commun.* **2024**, *38*, 108494. [CrossRef]
21. Brinker, C.J.; Scherer, G.W. CHAPTER 6—Aging of Gels. In *Sol-Gel Science*; Brinker, C.J., Scherer, G.W., Eds.; Academic Press: San Diego, CA, USA, 1990; pp. 356–405.
22. Kaptagay, G.A.; Satanova, B.M.; Abuova, A.U.; Konuhova, M.; Zakiyeva, Z.Y.; Tolegen, U.Z.; Koilyk, N.O.; Abuova, F.U. Effect of rhodium doping for photocatalytic activity of barium titanate. *Opt. Mater. X* **2025**, *25*, 100382. [CrossRef]
23. Ivanov, K.; Melnik, E.; Sirotkin, N.; Agafonov, A. The physicochemical properties of $BaTiO_3$/CuO nanocomposites and their photocatalytic activity under visible and UV light irradiation. *Opt. Mater.* **2025**, *168*, 117494.
24. Mohamed-Noriega, N.; Grothe, J.; Kaskel, S. Synthesis of Tetragonal $BaTiO_3$ Nanoparticles in Methanol. *Nanomaterials* **2025**, *15*, 1226.
25. Yu, J.; Jiang, Q.; Jia, Q.; Zhang, L.; Chiu, W.; Zeng, H. Designing a glass nanoshell on barium titanium trioxide to suppress nanocrystal growth during sintering for fine-grain dielectric ceramics. *J. Mater.* **2025**, *11*, 100883. [CrossRef]
26. Park, M.B.; Hwang, S.J.; Cho, N.H. Effect of the grain size and chemical features on the phase transition and physical characteristics of nano-grained $BaTiO_3$ ceramics. *Mater. Sci. Eng. B* **2003**, *99*, 155–158. [CrossRef]
27. Li, Q.L.; Chen, S.T.; Yao, P.; Wei, G.; Qu, Y.H. Thermal Decomposation Mecharism of the Nano-$BaTiO_2$ Formation. *Acta Phys.-Chim. Sin.* **2000**, *16*, 170–174. [CrossRef]
28. Tangwiwat, S.; Milne, S.J. Barium titanate sols prepared by a diol-based sol–gel route. *J. Non-Cryst. Solids* **2005**, *351*, 976–980. [CrossRef]
29. Wang, P.; Fan, C.; Wang, Y.; Ding, G.; Yuan, P. A dual chelating sol–gel synthesis of $BaTiO_3$ nanoparticles with effective photocatalytic activity for removing humic acid from water. *Mater. Res. Bull.* **2013**, *48*, 869–877. [CrossRef]
30. Mi, L.; Zhang, Q.; Wang, H.; Wu, Z.; Guo, Y.; Li, Y.; Xiong, X.; Liu, K.; Fu, W.; Ma, Y.; et al. Synthesis of $BaTiO_3$ nanoparticles by sol-gel assisted solid phase method and its formation mechanism and photocatalytic activity. *Ceram. Int.* **2020**, *46*, 10619–10633. [CrossRef]
31. Yoon, D.-H. Tetragonality of Barium Titanate Powder for a Ceramic Capacitor Application. *J. Ceram. Process. Res.* **2006**, *7*, 343–354.
32. Clabel H, J.L.; Awan, I.; Pinto, A.; Nogueira, I.; Bezzon, V.; Leite, E.; Balogh, D.; Mastelaro, V.; Ferreira, S.; Marega, E. Insights on the mechanism of solid state reaction between TiO_2 and $BaCO_3$ to produce $BaTiO_3$ powders: The role of calcination, milling, and mixing solvent. *Ceram. Int.* **2019**, *46*, 2987–3001. [CrossRef]
33. Luo, G.; Zhang, G.; Bai, L.; Zhang, Y.; Fan, Y.; Han, Y.; Guo, X.; Li, M.; Tu, R.; Shen, Q. Synthesis of tetragonal $BaTiO_3$ powder with size and dispersity optimization via synergy mechanisms of combined dispersants. *J. Alloys Compd.* **2023**, *944*, 169079. [CrossRef]
34. Ding, H.; Lin, L.; Gu, D.; Shang, S. Synthesis and surface modification of submicron $BaTiO_3$ powders via a facile surfactant-assisted method. *Ceram. Int.* **2020**, *46*, 22040–22048. [CrossRef]
35. Devi, L.G.; Krishnamurthy, G. TiO_2- and $BaTiO_3$-Assisted Photocatalytic Degradation of Selected Chloroorganic Compounds in Aqueous Medium: Correlation of Reactivity/Orientation Effects of Substituent Groups of the Pollutant Molecule on the Degradation Rate. *J. Phys. Chem. A* **2011**, *115*, 460–469. [CrossRef]
36. Perry, C.H.; Hall, D.B. Temperature Dependence of the Raman Spectrum of $BaTiO_3$. *Phys. Rev. Lett.* **1965**, *15*, 700–702. [CrossRef]

37. Cho, W.-S.; Hamada, E. Planar defects and luminescence of $BaTiO_3$ particles synthesized by a polymerized complex method. *J. Alloys Compd.* **1998**, *268*, 78–82. [CrossRef]
38. Tang, Z.; Zhou, Z.; Zhang, Z. Experimental study on the mechanism of $BaTiO_3$-based PTC–CO gas sensor. *Sens. Actuators B Chem.* **2003**, *93*, 391–395. [CrossRef]
39. Das, R.N.; Pramanik, P. Chemical synthesis of nanocrystalline lead zirconate-titanate powders using tartarate precursor. *Mater. Lett.* **1999**, *40*, 251–254. [CrossRef]
40. Tauc, J.; Grigorovici, R.; Vancu, A. Optical properties and electronic structure of amorphous germanium. *Phys. Status Solidi (b)* **1966**, *15*, 627–637.
41. Kaushik, V.; Kumar, V.; Kumar, D.; Kumar, R.; Singh, V.; Kumar, M.; Sharma, S.K. Effect of aging on microstructural and optical properties of sol-gel dip coated $BaTiO_3$ thin films. *Appl. Surf. Sci. Adv.* **2023**, *16*, 100418. [CrossRef]
42. Yao, Z.; Liu, H.; Liu, Y.; Wu, Z.; Shen, Z.; Liu, Y.; Cao, M. Structure and dielectric behavior of Nd-doped $BaTiO_3$ perovskites. *Mater. Chem. Phys.* **2008**, *109*, 475–481. [CrossRef]

Disclaimer/Publisher's Note: The statements, opinions and data contained in all publications are solely those of the individual author(s) and contributor(s) and not of MDPI and/or the editor(s). MDPI and/or the editor(s) disclaim responsibility for any injury to people or property resulting from any ideas, methods, instructions or products referred to in the content.